



Naturally derived carbon nanofibers as sustainable electrocatalysts for microbial energy harvesting: A new application of spider silk



Lihua Zhou^a, Peng Fu^a, Xixi Cai^b, Shungui Zhou^b, Yong Yuan^{b,*}

^a Institute of Natural Medicine & Green Chemistry, School of Chemical Engineering and Light Industry, Guangdong University of Technology, Guangzhou 510006, China

^b Guangdong Key Laboratory of Agricultural Environment Pollution Integrated Control, Guangdong Institute of Eco-Environmental and Soil Sciences, Guangzhou 510650, China

ARTICLE INFO

Article history:

Received 9 September 2015

Received in revised form 26 October 2015

Accepted 26 January 2016

Available online 30 January 2016

Keywords:

Spider silk

Carbon nanofibers

Electrocatalyst

Oxygen reduction reaction

Microbial fuel cell

ABSTRACT

Carbon nanofibers (CNFs) have drawn considerable attention as alternative catalysts for the oxygen reduction reaction (ORR). However, their facile, cheap, and environmentally friendly synthesis is still a great challenge. Herein, heteroatom-doped porous CNFs have been fabricated via a simple pyrolysis method using natural spider silk (SS) as a precursor. The prepared CNFs exhibit excellent ORR activity (half-wave potential of 0.85 V and on-set potential of 0.98 V vs RHE), superior to that of the Pt/C catalyst and most reported metal-free carbon catalysts in alkaline conditions. The catalytic proficiency is attributed to abundant electronegative N and S atoms within the carbon lattice, and a high surface area due to their nanofibrillar and porous structure. The prepared CNFs also exhibit excellent ORR activity in neutral solution (pH 7.0), showing potential application as cathode catalysts in microbial fuel cells (MFCs). An MFC equipped with the resulted CNF cathode presents a maximum power density of 1800 mW/m², 1.56 times higher than that with a Pt/C cathode. The performance of the resulting CNFs exceed that of other metal-free carbon catalysts in the current state of research on microbial energy harvesting.

© 2016 Elsevier B.V. All rights reserved.

1. Introduction

The oxygen reduction reaction (ORR) is one of the crucial reactions in fuel cells and other electrochemical devices, determining their efficiency and performance [1–3]. Electrocatalysts are necessary to accelerate the sluggish kinetics of the ORR. So far, the most efficient catalysts for the ORR are still platinum (Pt)-based materials. However, the widespread utilization of Pt-based catalysts is impractical due to their high costs, the scarcity of platinum and poisoning effects [4,5]. Recently, the incorporation of heteroatoms (i.e., nitrogen, sulfur, phosphorus, and boron) into carbon materials has been extensively investigated to provide alternatives to Pt-based catalysts due to their excellent catalytic activities, low costs, high tolerance to fuel poisoning and long-term stability [6,7]. Most of these studies focused on heteroatom-doped carbon nanotubes and graphene, some of which exhibited a comparable ORR performance to commercial Pt/C catalysts [8,9].

Carbon nanofibers (CNFs), another promising carbonaceous material with a cylindrical shape, have also drawn considerable attention as alternative catalysts for the ORR due to their unique textural and structural features. CNFs fabricated from temperate synthesis and electrospinning have been examined as potential electrocatalysts for the ORR [10,11]. The catalytic activity of CNFs can also be enhanced by heteroatom doping [12,13]. However, the need for relatively expensive, harmful precursors and tedious synthetic procedures are the major disadvantages to the large-scale production of these doped CNF materials. To mitigate these issues, an ideal solution is to achieve doped CNFs from widely available, accessible and recyclable biomass using cost-effective and eco-environmentally friendly methods. In this respect, Liang et al. reported a new type of N-doped CNF catalyst that is fabricated by the direct pyrolysis of bacterial cellulose, followed by N-doping by annealing in NH₃ [14]. However, the resulting N-doped CNFs still displayed lower activity for the ORR compared with the state-of-the-art Pt/C catalysts, and harmful NH₃ gas was needed for the activation.

Spider silk (SS), is a filamentous natural protein fiber (spidroins) made of repeated amino acid pattern that is known as one of the strongest natural materials [15]. Studies on the SS are gen-

* Corresponding author.

E-mail address: yuanrong@soil.gd.cn (Y. Yuan).

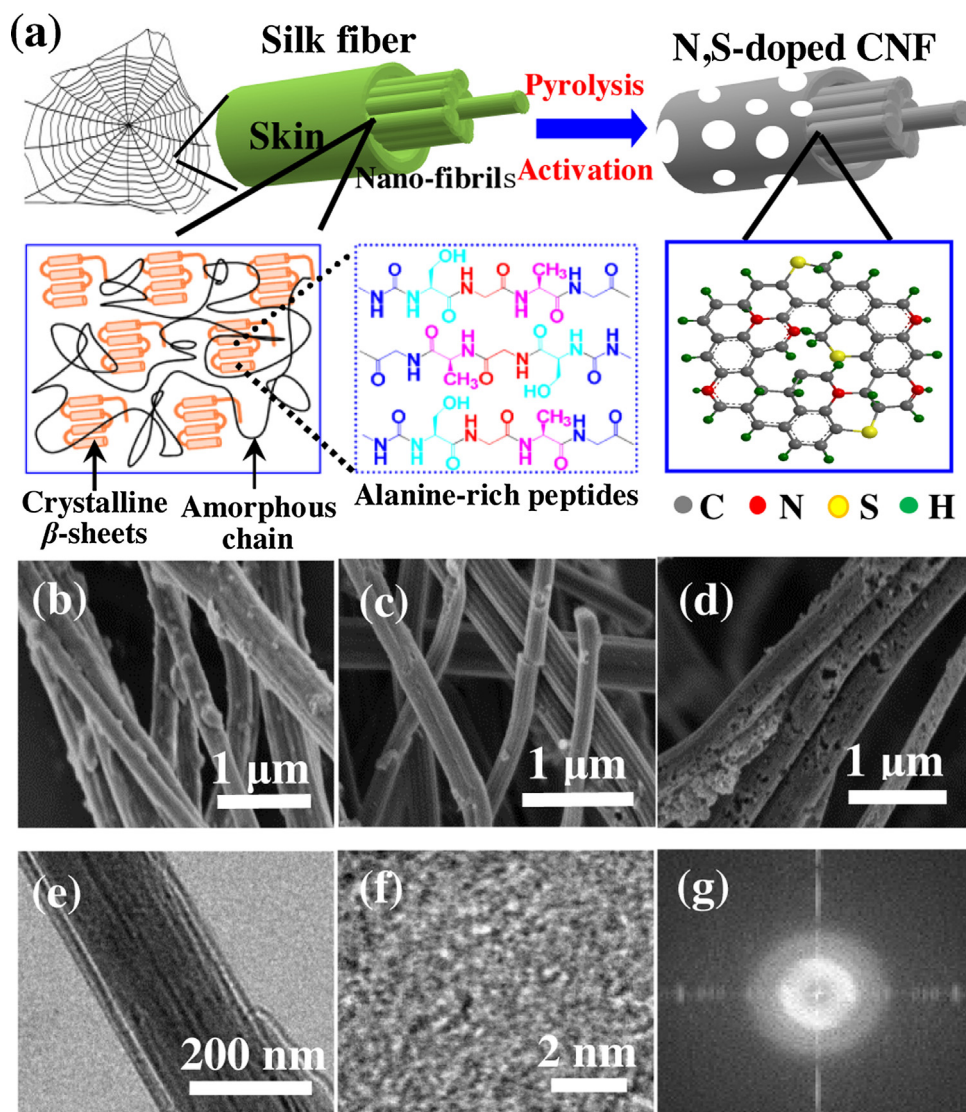


Fig. 1. (a) Schematic illustration of the procedures used for making SS-derived heteroatom-doped CNFs, the skin core structure of an individual dragline silk fiber, and compositions of a silk core fibril; SEM images of raw spider silks (b), S-CNF-900 (c) and SA-CNF-900 (d); TEM (e) and high-resolution TEM (f) images of SA-CNF-900; (g) SEAD pattern of SA-CNF-900.

erally focused on its applications in the biomedical and clinical fields due to its excellent biocompatibility and biodegradability [16]. Moreover, due to its sufficient flexibility and excellent mechanic properties, SS can serve as a versatile scaffold for functional nanomaterials used for fluorescent, magnetic and electronic applications [17–20]. However, it is worth mentioning that silk fibers are assemblies of highly oriented alanine-rich nanocrystals of antiparallel β -pleated sheets along the fiber axis and disordered glycine-rich peptide chains filled up the remaining fibrillar volume (Fig. 1a). The rich polypeptides of the natural SS indicates the high contents of C, N, and O elements, which might provide great opportunity for converting it into naturally derived heteroatom-doped carbon catalysts (Fig. 1a). Herein, for the first time, we fully utilized the chemical composition and fibrous structure of SS to convert it into heteroatom-doped porous CNFs through simple pyrolysis, following activation by the less harmful ZnCl_2 . The resulting activated CNFs showed excellent electrocatalytic activity for the ORR. By investigating the correlation between the structural variation and the ORR activity, we elucidated the ORR active sites of the CNFs. Finally, we also demonstrated that the SS-derived activated

CNFs (SA-CNFs) exhibited remarkable electrocatalytic activity for the ORR in microbial fuel cells (MFCs).

2. Experimental methods

2.1. Preparation of activated SS-derived carbon nanofibers (CNFs)

Natural spider silk (SS) samples produced by *Pholcus opilionoides* were collected from the local area and converted into carbon materials as depicted by Fig. S1. In brief, the obtained SS samples were washed with distilled water and then treated with 1 M HCl in an ultrasonic bath for 2 h to remove adsorbed impurities [21]. This process was repeated twice to ensure the complete elimination of any impurities on the SS samples. Then, the SS samples were washed with distilled water to remove the acid and dried at 30 °C for 24 h. The cleaned SS samples were then heated in an alumina crucible at 250 °C under a N_2 atmosphere for 2 h. The solid product was first dispersed into a 0.1 mol/L ZnCl_2 solution and then evaporated to dryness at 100 °C. The resulting solid samples were finally heated in an alumina crucible at 700, 800, 900, or 1000 °C under a

N₂ atmosphere for 2 h. The black product was collected after being treated with 1 M HCl solution under stirring for 24 h and washed with distilled water to remove any zinc impurities. The resulting carbon materials were termed SA-CNF-700, SA-CNF-800, SA-CNF-900, and SA-CNF-1000, respectively. For comparison, SS samples were also directly heated at 900 °C under a N₂ atmosphere for 2 h, and the resulting carbon materials were labeled S-CNF-900.

2.2. Physical characterization

The Brunauer-Emmett-Teller (BET) method was used to calculate the specific surface areas of the resulting carbon materials. The N₂ adsorption isotherm was measured at 77 K on a sorptometer (Model 1800, Carlo Erba Instruments, Italy). X-ray photoelectron spectroscopy (XPS) was performed using an X-ray photoelectron spectrometer (XPS, Kratos Model XSAM800) with a monochromatic Mg 300 W X-ray source. Fourier transform infrared (FTIR) spectra were measured on a Hitachi EPI infrared spectrophotometer. Field-emission scanning electron microscope (FE-SEM) images were obtained using a Hitachi S-4700 microscope (Hitachi, Ltd., Tokyo, Japan). High-resolution transmission electron microscope (HRTEM) images were obtained with a JEOL FE-2010 microscope operated at 200 kV.

2.3. Electrochemical measurements

The electrochemical measurements were carried out at room temperature in a conventional three-electrode cell connected to an electrochemical workstation (CHI660D, Shanghai Chenhua Instruments Co., China). A glassy carbon (GC) electrode (5.0 mm in diameter) coated with catalyst served as the working electrode. To prepare homogeneous catalyst inks, 2.0 mg of the as-prepared catalysts was dispersed in 1 mL mixed solution of 5% Nafion (Dupont)-ethanol-water. The catalyst ink (10 µL) was dropped onto the working electrode and dried at room temperature. A saturated calomel electrode (SCE) and a Pt wire were used as the reference and counter electrodes, respectively. The voltammetry experiments were conducted in an O₂-saturated 0.1 M KOH solution at room temperature at a scan rate of 10 mV s⁻¹. Rotating disk electrode (RDE) measurements were obtained with speeds varying from 800 to 2400 rpm at a scanning rate of 10 mV s⁻¹. Linear sweep voltammetry (LSV) curves were investigated by Koutecky-Levich (K-L) plots at various electrode potentials. The slopes of the best linear fit lines were used to calculate the number of electrons transferred (*n*) and the kinetic current densities from the K-L equation [22]:

$$\frac{1}{j} = \frac{1}{j_k} + \frac{1}{B\omega^{0.5}} \quad (1)$$

$$B = 0.62nF(D_{O_2})^{\frac{2}{3}}\nu^{-\frac{1}{6}}C_{O_2} \quad (2)$$

where *j* and *j_k* are the measured and kinetic limiting current densities, respectively, *ω* is the rotation speed, *n* is the number of electrons transferred in the reduction of one O₂ molecule, *F* is the Faraday constant (*F* = 96 485 C mol⁻¹), *D* is the diffusion coefficient of O₂ in 0.1 M KOH, *C* is the bulk O₂ concentration in 0.1 M KOH, and *ν* is the kinematic viscosity of the electrolyte (*ν* = 0.01 cm² s⁻¹).

2.4. MFC setup and operation

Cubic air-cathode single-chamber microbial fuel cells (MFCs) were set up as previously described by Watson et al. [23]. The anode was a graphite fiber brush (2.5 cm in both diameter and length) with a core of two twisted titanium wires that functioned as a current collector, which was placed horizontally in the middle of the cylindrical chamber. The cathode was placed at the other side of

the reactor, with the diffusion layers facing the air. All the MFCs were inoculated with the effluent of MFCs that were well operated for over half a year. The medium was 1 g/L sodium acetate solution in a 50 mM phosphate buffer (pH 7.0, PBS) supplemented with a 12.5 mL/L mineral solution and a 5 mL/L vitamin solution. All MFCs were operated in batch mode in a 30 °C incubator. Initially, Pt/C cathodes were used for all the MFCs during the start-up to ensure that the anodes achieved the same performance during the acclimation. After a repeatable cycle of voltage was produced by the MFCs, the Pt/C cathodes were removed and replaced with the new CNF-based cathodes. The catalyst dosage on the cathode surface was 2 mg/cm² for the carbon nanofibers and 0.5 mg/cm² for Pt (20% Pt/C). The voltages of the MFCs were recorded using a multi-channel voltage collection instrument (AD8223, Ruibohua Control Technology Co., Ltd., Beijing, China) with a 1 kΩ external resistance (except as noted). The polarization curve was constructed by discharging the cell with external loads of various resistances. The anode and cathode potential of MFC was measured by using a multimeter and a reference electrode (SCE) located in the middle of the fuel cell chamber. All MFCs were operated in triplicate, and the mean values are presented in this study. The current densities and power densities were normalized by the projected surface area of the cathode (7.0 cm²). All of the tests were conducted in batch mode in a 30 °C incubator.

3. Results and discussion

3.1. Preparation of SS-derived porous heteroatom-doped CNFs

Natural SS samples were collected from the local area and converted into carbon materials, as depicted by Fig. S1. Fig. 1b–d shows typical SEM images of SS samples as collected, together with the heat-treated silks. The fiber structure of the silk can be observed in the SEM images, exhibiting 1-D structures with a diameter of 200–400 nm. The fibers maintained their continuous filament morphology after carbonization (Fig. 1 and Fig. S2). However, it can be seen from the SEM images (Fig. 1d) that many visible micropores are distributed on the activated CNFs, which is a result of the activation by ZnCl₂. It is worth noting that the nanofiber structure is well maintained after activation, indicating that the activation is mild enough to maintain the nanofiber coherency. Figs. S2d and e shows the remained skin-core structure and interior fibrous core region of the resulting CNF with irregular protrusions along the fibre axis, respectively. The nanofiber structure of the SS-derived activated carbon nanofibers (SA-CNFs) was also confirmed by TEM (Fig. 1e). A high-resolution TEM image reveals that the nanofiber surface exhibits small porous networks (Fig. 1f). SAED of the CNFs shows diffuse rings in the diffraction pattern (Fig. 1g), which indicates that the sample is amorphous [24].

3.2. Characterization of the SS-derived CNFs

Fig. 2a shows the Brunauer-Emmett-Teller (BET) isotherm of the SA-CNFs at various temperatures (labeled as SA-CNF-x, x representing the pyrolysis temperature). Remarkable hysteresis loops were observed from the activated carbon nanofibers, which indicated the mesoporous nature of these materials. The BET surface areas of the activated carbon nanofibers at different temperatures were 142.5 m²/g (SA-CNF-700), 383.0 m²/g (SA-CNF-800), 721.6 m²/g (SA-CNF-900), and 552.6 m²/g (SA-CNF-1000), all of which are much higher than that of the SS-derived carbon nanofibers without activation (labelled as S-CNF-900, 60 m²/g) (Table S1). Fig. 2b is the pore size distribution of the samples, which shows that the size range of the pores is mainly from 1 to 20 nm. The corresponding pore size distributions of the mesopores are centered at 1.0,

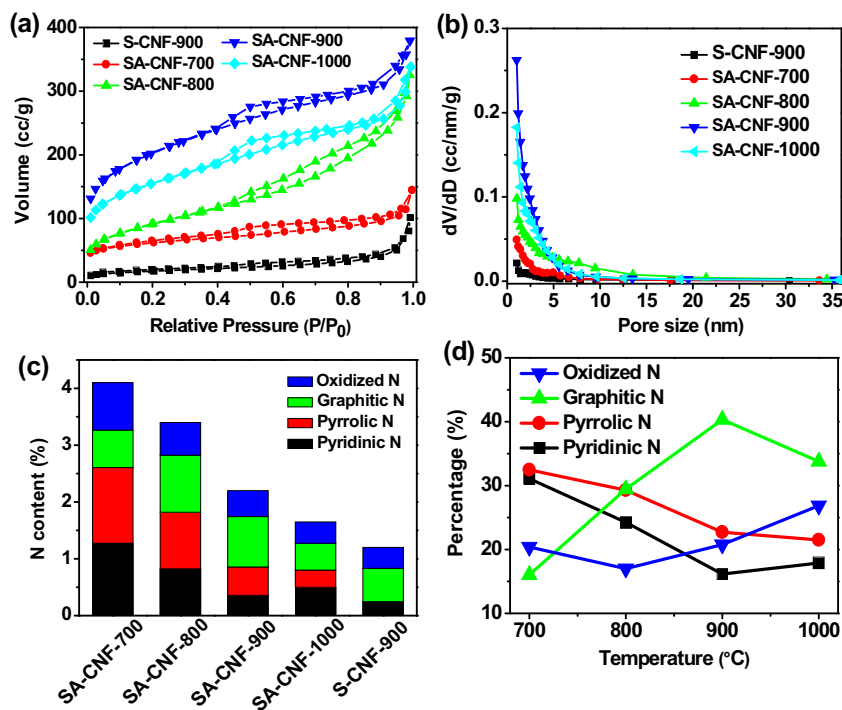


Fig. 2. (a) Nitrogen adsorption–desorption isotherms for SS-derived CNFs; (b) Pore size distributions for the resulting CNFs; (c) The contents of four types of nitrogen in the SS-derived CNFs; (d) nitrogen content of the CNFs as a function of the pyrolysis temperature.

5.4, 5.6, 3.8, and 3.2 nm (Table S1). The total pore volumes are 0.19, 0.53, 0.99, and 0.52 cm^3/g for SA-CNF-700, SA-CNF-800, SA-CNF-900, and SA-CNF-1000, respectively, all of which are higher than that of S-CNF-900 (0.16 cm^3/g). The results suggest that chemical activation is a useful strategy to increase the surface area of the SS-derived CNFs by creating mesopores on the nanofibers. Comparing the surface area and pore volume of all the activated CNFs derived at different temperatures, it is suggested that 900 $^{\circ}\text{C}$ is a suitable temperature to achieve the highest surface area.

The conversion of the SS into carbonaceous materials was also confirmed by FT-IR and XPS measurements. The FT-IR spectra of the raw SS and carbonized materials are shown in Fig. S2d. Raw SS showed abundant carboxyl and hydroxyl groups, as indicated by the presence of absorption bands in the region from 300 to 4000 cm^{-1} . There is also an absorption band related to the stretching of the N–H bond of organic compounds in this region of the spectrum. Absorption bands at 1545 and 1650 cm^{-1} contributed to the C=O vibration of the primary amides [25]. The FT-IR spectra of S-CNF-900 and SA-CNF-900 were nearly identical, showing a broad continuum absorption with only a few peaks over the range of 500–4000 cm^{-1} . These properties are due to the excitation of the “free” conducting electrons [26].

XPS measurements were employed to reveal the chemical structure of the SA-CNFs. The XPS survey spectra revealed the presence of C, O, N, and S in the SS and CNFs (Fig. S3). The XPS data showed the atomic percentages of C (61.3%), O (18.9%), N (6.8%), and S (1.1%) in the SS (Table S1). After heat treatment, the atomic percentage of C increased, and the atomic percentages of the other elements decreased. The deconvoluted high-resolution spectra of raw SS, S-CNF-900 and SA-CNF-900 are shown in Figs. S3 and S4. In the high-resolution C 1s spectrum of SS, the dominant peak at 284.6 eV can be attributed to the C–C and C=C bonds, whereas the peak at 286.2 eV is attributed to the C–O or C=N bonds and the peak at 287.9 eV is attributed to the C=O or C–N bonds (Fig. S3b) [27]. After being carbonized, fewer peaks were observed for the C 1s spectrum of S-CNF-900, demonstrating the

increase in the content of C–C bonds in graphitic carbon. In the high-resolution O1s spectra (Fig. S3c), three peaks were observed for both the SS and CNFs, which were identified as the O–C bond (532.9–533.2), O=C bond (531.7–532.2 eV), and O–H bond (530.5–531.0 eV), respectively [28]. From the high-resolution N1s spectra (Fig. S4a), pyridinic (N1, 398.1 eV), pyrrolic (N2, 399.7 eV), and graphitic (N3, 400.8 eV) groups were observed on the structure of the SS samples, whereas pyridinic (N1, 398.1 eV), graphitic (N3, 400.8 eV) and oxidized nitrogen-containing (N4, 402.0 eV) groups were doped on the resulting S-CNF-900. Pyridinic (N1, 398.1 eV), pyrrolic (N2, 399.7 eV), graphitic (N3, 400.8 eV) and oxidized nitrogen-containing (N4, 402.0 eV) groups were doped on the resulting SA-CNF-900 (Fig. 2c and Fig. S4). To investigate the transformation of the N groups during pyrolysis, the percentages of N groups in carbon materials prepared at different temperatures are plotted in Fig. 2c and d. As shown in the figures, the total N percentage decreased as the temperature increased, and a conversion from pyridinic and pyrrolic N to the more stable graphitic N upon increasing the pyrolysis temperature was observed, which is consistent with a previous report on N-doped carbon materials [29]. The high-resolution S 2p spectrum can be resolved into two different peaks at approximately 164 and 168 eV, which are attributed to thiophene-S and oxidized S groups, respectively (Fig. S4b) [30]. The peak of the thiophene-S in the SS is very small compared with that of the oxidized S, indicating that the oxidized S groups are dominant. The oxidized S groups can result from the cysteine residues of the N-terminal sequences in the polypeptides of the natural SS [31]. These cysteines may participate in intra- or inter-molecular disulfide bridges in the heavy-chain fibroin [32]. However, after pyrolysis, the peak intensity of the thiophene-S is significantly increased, confirming the conversion of the oxidized S to S–C groups in the carbonized SS nanofibers. The S–C groups have been previously demonstrated to play important roles in the catalytic activity of the carbon catalyst for the ORR due to their high charge densities [9]. The densities and distributions of these heteroatoms on SA-CNF-900 were evaluated by quantitative energy

dispersive X-ray spectroscopy (EDS). As seen in Fig. S5, these elements were homogeneously distributed over the surface, which could be beneficial for the catalytic activity of the resulting catalyst.

3.3. Electrocatalytic properties of CNFs toward ORR

The as-prepared heteroatom-doped CNFs were evaluated for the electrocatalytic ORR. The cyclic voltammogram (CV) of the SA-CNF-900 electrode showed the typical pseudo-capacitive behavior of heteroatom-doped graphitic carbon in the N_2 -saturated 0.1 M KOH electrolyte (Fig. 3a). In contrast, a well-defined cathodic current peak at -0.18 V vs. SCE was observed from the O_2 -saturated KOH solution, indicating the electrocatalytic activity of SA-CNF-900 for the ORR. To better understand the electrochemical performance of SA-CNF-900 during the ORR process, linear sweep voltammograms (LSVs) were obtained on a rotating disc electrode by scanning the potential from 0.2 to -0.8 V at a rotation rate of 1600 rpm and scan rate of 10 mV/s. It was found that SA-CNF-900 has an onset potential of -0.03 V vs. SCE (0.98 vs. RHE) and a half-wave potential of -0.16 V vs. SCE (0.85 vs. RHE) (Fig. 3b). Remarkably, SA-CNF-900 displayed the most positive onset potential and highest reaction current density compared to the other CNF samples such as S-CNF-900, SA-CNF-700, SA-CNF-800, and SA-CNF-1000. It is worth noting that SA-CNF-900 shows even more positive onset potential and higher reaction current density than those of commercial Pt/C (Fig. 3b) and previously reported synthesized or biomass-derived carbon metal-free catalysts. (Table S2 and S3). The catalytic activity of SA-CNF-900 is much higher than that of S-CNF-900, demonstrating that the chemical activation is a very valid approach to increase the catalytic activity of the SS-derived CNFs. As revealed by physical and chemical measurements, the increased surface area and higher N-atom content should be reasons for the enhanced catalytic activity of SA-CNF-900 compared with S-CNF-900. The annealing temperature is another key parameter enabling the production of highly active carbon nanofibers for the ORR from the SS, which can affect both the surface area and heteroatom content of the carbon nanofibers. The highest surface area and graphitic N content were achieved by SA-CNF-900 compared with the other samples treated at other temperatures, which could contribute to its highest catalytic activity.

To further compare the ORR performances of all the samples, RDE measurements were also performed at different rotational speeds from 800–2400 rpm (Fig. 3c and Fig. S6). The kinetic parameters, such as the electron-transfer number (n) and kinetic current density (j_k), of all the samples were analyzed on the basis of K-L plots. Fig. 3d and Fig. S6 profile the corresponding K-L plots that demonstrate the inverse current density (j^{-1}) as a function of the inverse of the square root of the rotation speed ($\omega^{-1/2}$) at different potential values. In the K-L plots of SA-CNF-900, the relationship between $1/j$ and $\omega^{-1/2}$ was linear between -0.3 V and -0.7 V. According to the K-L equations, the number of electrons transferred during the ORR process for SA-CNF-900 was close to four, indicating that the ORR process occurred via a four-electron transfer pathway, which is similar to that of the commercial Pt/C catalyst (Fig. 3e). Notably, the number of electrons transferred for S-CNF-900 was approximately 3.2–3.8, indicating that the ORR process occurred via a combined two and four-electron transfer pathway. In addition, the j_k value at -0.2 V vs. SCE is 18.5 mA cm^{-2} for the SA-CNF-900, which is superior to those of S-CNF-900 (0.2 mA cm^{-2}), SA-CNF-700 (0.8 mA cm^{-2}), SA-CNF-800 (2.7 mA cm^{-2}), SA-CNF-1000 (4.9 mA cm^{-2}), and Pt/C (12.4 mA cm^{-2}) (Fig. 3f). Relative to other samples, the more positive the onset potential, the higher the kinetic current density, and the higher electron-transfer number for SA-CNF-900 should be attributed to its porous structure and the proposed synergistic effect caused by the N and S doping, as these heteroatoms introduced into the carbon lattice can change

not only the carbon surface chemistry but also its electronic structure [33,34]. The catalytic activity of the resulting carbon materials varied with the pyrolysis temperatures (Fig. 3b). The variation in the catalytic activity of the CNFs with different pyrolysis temperatures is in accordance with the fluctuation of the graphitic N content (Fig. 2d), suggesting that graphitic N is the primary N functionality for the ORR catalytic activity in the SA-CNFs.

Heteroatom-doped metal-free carbon materials commonly show better stability and tolerance to the crossover effect than the Pt/C catalyst. The stability and tolerance to methanol of SA-CNF-900 was examined during the ORR process. As shown in Fig. S7a, the catalytic current of SA-CNF-900 for the ORR was unaffected by the addition of 3 M methanol, whereas a strong amperometric response was observed for Pt/C as a result of methanol addition during the ORR process. In addition, the ORR current density of SA-CNF-900 electrode decreased by only 7.3% over 10,000 s of continuous operation at -0.4 V vs. SCE, while the Pt/C catalyst exhibited a 33.3% decrease in current density under similar testing conditions (Fig. S7b). These results suggest that the SS-derived activated carbon nanofibers exhibit a promising stability and selectivity towards the ORR with a remarkable tolerance to crossover effects.

3.4. Application of SA-CNF-900 as the cathode catalyst for microbial energy harvesting

Recent advancements in the ORR suggest that metal-free carbon materials could work as efficient catalysts for the ORR in microbial fuel cells (MFCs) [5]. MFCs are an emerging renewable energy technology to directly recover electrical energy from wastewater using bacteria as catalysts, to simultaneously treat wastewater and harvest electrical energy [35,36]. However, the commercial applications of MFCs have been baffled by the cost and stability of the Pt cathode. Herein, SA-CNF-900 was evaluated as an advanced catalyst to replace the high-cost Pt in a single-chamber MFC. However, it is noteworthy that MFCs are usually operated with a near neutral electrolyte pH to maintain optimal conditions for bacterial growth. Therefore, the ORR performance of the SA-CNF-900 was also investigated in neutral solution (pH 7.0). As shown in Fig. 4a, the SA-CNF-900 shows well-defined cathodic ORR peaks in O_2 -saturated 50 mM PBS (pH 7.0), suggesting the electrocatalytic activity of the SA-CNF-900. The SA-CNF-900 showed a slightly negative ORR peak potential (0.09 V vs. SCE) compare to that of the Pt/C (0.12 V vs. SCE), but presented a higher cathodic current than that of the Pt/C. To further investigate the ORR performance, we carried out the LSV measurements on a RDE for all CNFs samples in O_2 -saturated PBS. Similarly, SA-CNF-900 also displayed the most positive onset potential and highest reaction current density compared to other CNF samples in O_2 -saturated neutral solution (Fig. 4b). It is noticed that the limiting current density of the SA-CNF-900 is very similar to that of the Pt/C catalyst, suggesting the excellent electrochemical activity of the SA-CNF-900 for ORR in neutral solution. As presented in Fig. 4c, the current density of the SA-CNF-900 increased as the rotation rate increased from 800 to 2400 rpm. The K-L plots at the potential of -0.1 , -0.2 , -0.3 and -0.4 V were obtained and displayed good linearity (Fig. 4d). The n value for the SA-CNF-900 was calculated to be $3.7 \sim 4.0$, indicating that the SA-CNF-900 is effective for a 4-electron ORR in O_2 -saturated PBS, which is similar to that of the Pt/C (Fig. S8a–c).

The suitability of the SA-CNF-900 for the MFC cathode was further explored by revealing the crossover effect of typical microbial substrates and metabolites (e.g. formate, ethanol, lactate, methanol, acetate, sulphide, and ascorbate) on the limiting oxygen reduction current densities. As shown in Fig. S8d, it is demonstrated that the performance of the Pt/C is substantially diminished in the presence of these compounds except acetate, which is in accordance with previous study [37]. However, the ORR performance at

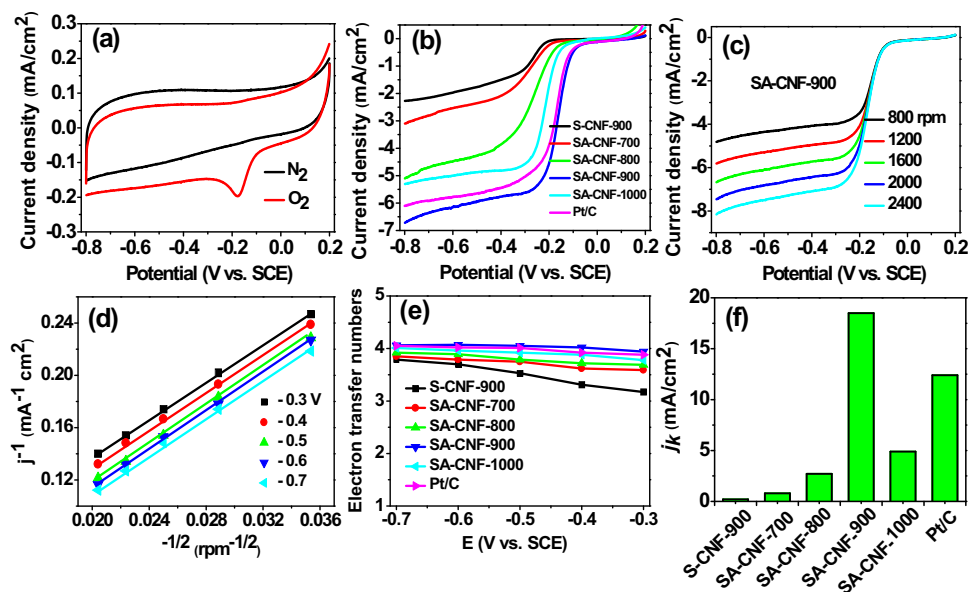


Fig. 3. (a) CV curves for SA-CNF-900 in N_2 -saturated and O_2 -saturated 0.1 M KOH solutions at a scan rate of 10 mV s^{-1} ; (b) RDE curves for CNFs and Pt/C with a rotation speed of 1600 rpm; (c) RDE curves for SA-CNF-900 at different rotation rates; (d) K-L plots at different potentials for SA-CNF-900; (e) the calculated number of electrons transferred (n); (f) Comparison of the kinetic current density (j_k) of the ORR at -0.2 V on various CNF materials and Pt/C.

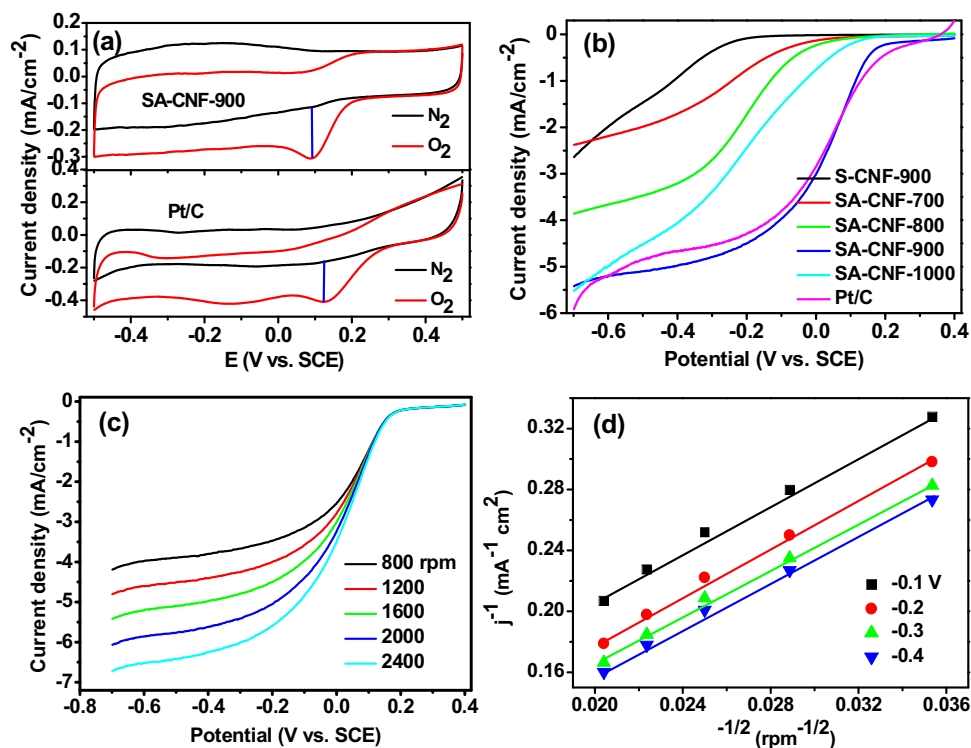


Fig. 4. (a) CV of SA-CNF-900 and Pt/C in N_2 -saturated and O_2 -saturated 50 mM PBS; (b) LSVs for CNFs and Pt/C in O_2 -saturated PBS at a rotation speed of 1600 rpm; (c) LSVs for SA-CNF-900 at different rotation rates; (d) K-L plots at different potentials for SA-CNF-900 in O_2 -saturated PBS.

the SA-CNF-900 remains unaffected in the presence of these compounds, suggesting the excellent stability of this material for the ORR. It is noteworthy that the ORR performance of both materials is substantially deteriorated by the presence of ascorbate. This may be attributed to the catalytic oxidation of ascorbate by the Pt/C and the SA-CNF-900.

Finally, the feasibility of the SA-CNF-900 was investigated as a catalyst for ORR in an air-cathode MFC. After the cell voltages were stabilized, the MFCs were subjected to polarization analyses (Fig.

S9). As shown in Fig. 5a, the MFC with the SA-CNF-900 cathode had a maximum power density of $1800 \pm 82 \text{ mW/m}^2$, which was approximately 1.56 times higher than that of the MFC with the Pt/C cathode catalyst ($1152 \pm 73 \text{ mW/m}^2$). Fig. 5b shows the potential vs. current density curves for the individual cathodes and anodes. For these MFCs, the cathode potentials were different, while the anode potentials were similar, indicating that the differences in the MFC performances primarily resulted from variations in the catalytic activities of the cathode catalysts. Stability tests showed

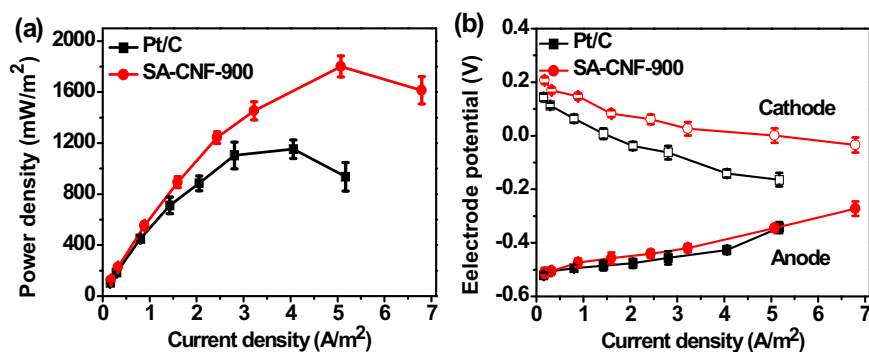


Fig. 5. (a) Polarization curves of MFCs with SA-CNF-900 and Pt/C cathodes; (b) Curves of individual potential (vs SCE reference electrode: 0.244 V vs standard hydrogen electrode SHE) in MFCs.

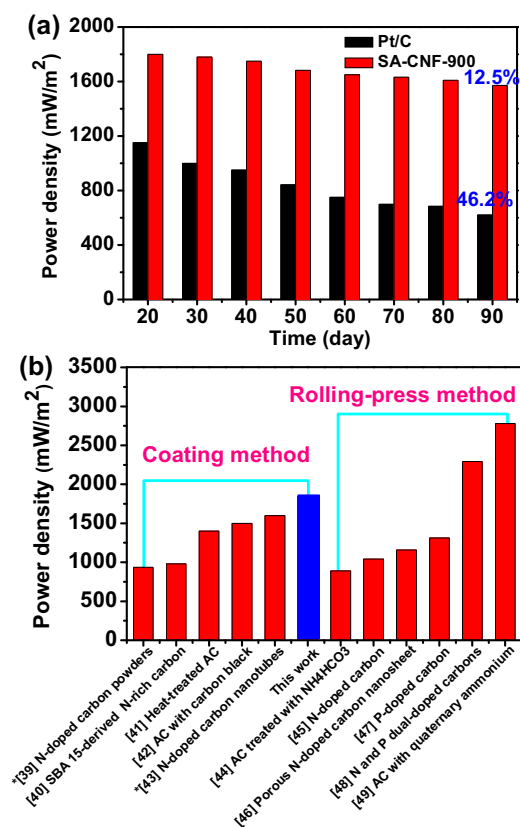


Fig. 6. (a) The maximum power densities of the MFCs with different catalysts during long-term operations; (b) Comparison of SA-CNF-900 with that of the current state-of-the-art non-metal carbon catalysts for the power densities in air-cathode single-chamber MFCs.

that SA-CNF-900 was highly stable, with only a 12.5% decline in the power output over 3 months operation, which outperformed the Pt/C with a 46.2% decline in the power output (Fig. 6a).

The MFC performance with the SA-CNF-900 cathode can out-compete those with other reported non-metal carbonaceous catalysts in the current state of research (Fig. 6b). It is difficult to directly compare the performance of the MFCs because the experimental conditions are not exactly the same across all the MFC systems. To be more reasonable, we made the comparison based on similar MFC configurations (cylindrical chamber of 4 cm in length by 3 cm in diameter) and operating conditions, including the electrolyte (50 mM phosphate buffer), anode electrode (graphite brush), inoculum (mixed culture) and reactor size (liquid volume 28 mL and a projected surface area of the cathode

of 7 cm², with the only two exceptions indicated by asterisks). Note that two methods were generally used to prepare the cathodes: coating and rolling-press methods. As previously reported by Wang et al., the rolling-press method was better than the coating method [38]. However, a relatively complicated process and special rolling machine was required for the rolling-press method. Herein, we used the simple coating method to load the non-metal carbon nanofiber catalysts onto the cathode. The highest power density was achieved from the MFC with our carbon nanofiber cathode compared to the other carbon cathodes fabricated with the coating method [39–43]. The performance of the carbon nanofiber cathode from the coating method is comparable to that of state-of-the-art carbon cathodes from the rolling-press method [44–49].

demonstrating the suitability of the resulting carbon nanofibers as a potential alternative to Pt/C for microbial energy harvesting.

4. Conclusions

In summary, we have revealed that metal-free SS-derived CNFs exhibit exceptionally high catalytic activity for the ORR. The catalytic proficiency of the SS-derived CNFs is attributed to the highly positive charges on the carbon atoms due to the presence of the electronegative nitrogen and sulfur atoms within the carbon lattice. The extremely high ORR performance of the SS-derived CNFs is attributed to their high surface area and large number of active sites due to their nanofibrillar structure and abundant mesopores. An MFC using SA-CNF-900 as the cathode catalyst produced a power density 1.56 times higher than that using a commercial Pt/C catalyst, suggesting that SA-CNFs are a good alternative to commercial Pt/C catalysts for microbial energy harvesting. The present study provides a new route for the direct preparation of CNF electrocatalysts with high activity and low cost.

Acknowledgements

Financial support was provided by Guangdong Natural Science Funds for Distinguished Young Scholar (2014A030306033), National Natural Science Foundation of China (Grant No. 41301264 and 21277035), and Major Science and Technology Project of Guangdong Province (2012A010800003).

Appendix A. Supplementary data

Supplementary data associated with this article can be found, in the online version, at <http://dx.doi.org/10.1016/j.apcatb.2016.01.063>.

References

- [1] B.C.H. Steele, A. Heinzel, *Nature* 414 (2001) 345–352.
- [2] K. Gong, F. Du, Z. Xia, M. Dustock, L. Dai, *Science* 323 (2009) 760–764.
- [3] Y.G. Li, M. Gong, Y.Y. Liang, J. Feng, J.E. Kim, H.L. Wang, G.S. Hong, B. Zhang, H.J. Dai, *Nat. Commun.* 4 (2013) 1805.
- [4] A. Rinaldi, B. Mecheri, V. Garavaglia, S. Licocchia, P.D. Nardo, E. Traversa, *Energy Environ. Sci.* 1 (2008) 417–429.
- [5] X. Liu, W. Li, H.Q. Yu, *Chem. Soc. Rev.* 43 (2014) 7718–7745.
- [6] Z. Yang, H. Nie, X. Chen, X. Chen, S. Huang, *J. Power Sources* 236 (2013) 238–249.
- [7] L. Dai, Y. Xue, L. Qu, H.J. Choi, J.B. Baek, *Chem. Rev.* 115 (2015) 4823–4892.
- [8] Y. Yan, J. Miao, Z. Yang, F. Xiao, H. Yang, B. Liu, Y. Yang, *Chem. Soc. Rev.* 44 (2015) 3295–3346.
- [9] X. Kong, C. Chen, Q. Chen, *Chem. Soc. Rev.* 43 (2014) 2841–2857.
- [10] J. Zheng, X. Zhang, P. Li, X. Zhou, D. Chen, Y. Liu, W. Yuan, *Electrochim. Acta* 53 (2008) 3587–3596.
- [11] J. Zheng, X. Zhang, P. Li, X. Zhou, W. Yuan, *Catal. Today* 131 (2008) 270–277.
- [12] S. Maldonado, K.J. Stevenson, *J. Phys. Chem. B* 109 (2005) 4707–4716.
- [13] D. Liu, X. Zhang, T. You, *J. Power Sources* 273 (2015) 810–815.
- [14] H. Liang, Z. Wu, L. Chen, C. Li, S. Yu, *Nano Energy* 11 (2015) 366–376.
- [15] J.A. Kluge, O. Rabotyagova, G.G. Leisk, D.L. Kaplan, *Trends Biotechnol.* 26 (2008) 244–251.
- [16] I. Agnarsson, A. Dhinojwala, V. Sahni, T.A. Blackledge, *J. Exp. Biol.* 212 (2009) 1990–1994.
- [17] M. Chu, Y. Sun, *Smart Mater. Struct.* 16 (2007) 2453–2456.
- [18] E.L. Mayes, F. Vollrath, S. Mann, *Adv. Mater.* 10 (1998) 801–805.
- [19] E. Steven, J.G. Park, A. Paravastu, E.B. Lopes, J.S. Brooks, O. Englander, T. Siegrist, P. Kaner, R.G. Alamo, *Sci. Technol. Adv. Mater.* 12 (2011) 35.
- [20] E. Steven, W.R. Saleh, V. Lebedev, S.F.A. Acquah, V. Laukhin, R.G. Alamo, J.S. Brooks, *Nat. Commun.* 4 (2013) 2435.
- [21] L. Pelita, F.N. Ertas, A.E. Eroglu, T. Shahwan, H. Tural, *Bioresour. Technol.* 102 (2011) 8807–8813.
- [22] S. Yang, L. Zhi, K. Tang, X. Feng, J. Maier, K. Müllen, *Adv. Funct. Mater.* 22 (2012) 3634–3640.
- [23] V.J. Watson, C.N. Delgado, B.E. Logan, *Environ. Sci. Technol.* 47 (2013) 6704–6710.
- [24] J. Wang, C. Wang, S. Chen, *Angew. Chem. Int. Ed.* 51 (2012) 9297–9301.
- [25] J.O. Silva, G.R. Filho, C.S. Meireles, S.D. Ribeiro, J.G. Vieira, C.V. Silva, D.A. Cerqueira, *Thermochim. Acta* 528 (2012) 72–75.
- [26] J.J. Langer, S. Golczak, P.D. Stab, *Polym. Degrad. Stab.* 92 (2007) 330–334.
- [27] T.I.T. Okpalugo, P. Papakonstantinou, H. Murphy, J. McLaughlin, N.M.D. Brown, *Carbon* 43 (2005) 153–161.
- [28] V. Datsyuk, M. Kalyva, K. Papagelis, J. Parthenios, D. Tasis, A. Siokou, I. Kallitsis, C. Galiotis, *Carbon* 46 (2008) 833–840.
- [29] Z. Lin, G.H. Waller, Y. Liu, M. Liu, C. Wong, *Nano Energy* 2 (2013) 241–248.
- [30] Z. Ma, S. Dou, A. Shen, L. Tao, L. Dai, S. Wang, *Angew. Chem. Int. Ed.* 54 (2015) 1888–1892.
- [31] J. Garb, N. Ayoub, C. Hayashi, *BMC Evol. Biol.* 10 (2010) 243.
- [32] X. Hu, K. Kohler, A.M. Falick, A.M.F. Moore, P.R. Jones, C. Vierra, *Biochem.* 45 (2006) 3506–3516.
- [33] H. Zhang, Y. Wang, D. Wang, Y. Li, X. Liu, P. Liu, H. Yang, T. An, Z. Tang, H. Zhao, *Small* 10 (2014) 3371–3378.
- [34] Y. Li, H. Zhang, Y. Wang, P. Liu, H. Yang, X. Yao, D. Wang, Z. Tang, H. Zhao, *Energy Environ. Sci.* 7 (2014) 3720–3726.
- [35] B.E. Logan, J.M. Regan, *Environ. Sci. Technol.* 40 (2006) 5172–5180.
- [36] W. Li, H. Yu, Z. He, *Energy Environ. Sci.* 7 (2014) 911–924.
- [37] F. Harnisch, S. Wirth, U. Schröder, *Electrochem. Commun.* 11 (2009) 2253–2256.
- [38] H. Dong, H. Yu, X. Wang, Q. Zhou, J. Feng, *Water Res.* 46 (2012) 5777–5787.
- [39] X. Shi, Y. Feng, X. Wang, H. Lee, J. Liu, Y. Qu, W. He, S.M. Kumar, N. Ren, *Bioresour. Technol.* 108 (2012) 89–93.
- [40] I. Ivanov, T.C. Nagaiah, A. Bordoloi, B.E. Logan, *J. Power Sources* 269 (2014) 212–215.
- [41] X. Zhang, D. Pant, F. Zhang, J. Liu, W. He, B.E. Logan, *ChemElectroChem* 1 (2014) 1859–1866.
- [42] X. Zhang, X. Xia, I. Ivanov, X. Huang, B.E. Logan, *Environ. Sci. Technol.* 48 (2014) 2075–2081.
- [43] L. Feng, Y. Yan, Y. Chen, L. Wang, *Energy Environ. Sci.* 4 (2011) 1892–1899.
- [44] D. Lia, Y. Qu, J. Liu, W. He, H. Wang, Y. Feng, *J. Power Sources* 272 (2014) 909–914.
- [45] G. Yu, K. Meng, Q. Liu, *ChemPlusChem* 80 (2015) 1133–1138.
- [46] Q. Wen, S. Wang, J. Yan, L. Cong, Y. Chen, H. Xi, *Bioelectrochem.* 95 (2014) 23–28.
- [47] Q. Liu, S. Chen, Y. Zhou, S. Zheng, H. Hou, F. Zhao, *J. Power Sources* 261 (2014) 245–248.
- [48] Q. Liu, Y. Zhou, S. Chen, Z. Wang, H. Hou, F. Zhao, *J. Power Sources* 273 (2015) 1189–1193.
- [49] X. Wang, C. Feng, N. Ding, Q. Zhang, N. Li, X. Li, Y. Zhang, *Environ. Sci. Technol.* 48 (2014) 4191–4198.